Linking SO_2 emission rates and seismicity by continuous wavelet transform: Implications for volcanic surveillance at San Cristobal volcano, Nicaragua

Corresponding author: Vladimir Conde

Department of Earth and Space Sciences, Chalmers University of Technology

Hörsalsvägen 11, 412 96, Gothenburg, Sweden

conde@chalmers.se

Tel: +46 31 7721 1589

Fax: +46 31 772 1884

Stefan Bredemeyer

SFB 574 and GEOMAR Helmholtz Centre for Ocean Research Kiel

Wischhofstr. 1-3, 24118, Kiel, Germany

sbredemeyer@geomar.de

J. Armando Saballos

Instituto Nicaraguese de Estudios Territoriales (INETER)

Apdo. Postal 2110, Managua, Nicaragua.

armando.saballos@gf.ineter.gob.ni

Bo Galle

Department of Earth and Space Sciences, Chalmers University of Technology

Hörsalsvägen 11, 412 96, Gothenburg, Sweden

bo.galle@chalmers.se

Thor H. Hansteen

GEOMAR Helmholtz Centre for Ocean Research Kiel

Wischhofstr. 1-3, 24118, Kiel, Germany

thansteen@geomar.de

Keywords

DOAS, volcanic SO_2, RSAM, wavelets, CWT and XWT

Abstract

San Cristobal volcano is the highest and one of the most active volcanoes in Nicaragua. Its persistently high activity is characterized by strong degassing and relatively frequent explosive eruptions, and thus demands multi-parameter surveillance efforts of local institutions. After September 2012, a series of moderately explosive eruptions heralded the start of a new eruptive phase characterized by pulsating activity. The eruptions were accompanied by increasing gas emissions and seismicity.

As a part of the Network for Observation of Volcanic and Atmospheric Change project, two permanent instruments using the UV-DOAS technique were installed aiming to make measurements of SO_2 emissions. We present here the results of semi-continuous gas flux measurements mainly over a period of about two years, including the recent anomalies. Correspondingly we demonstrate how the joint analysis of continuous SO_2 flux measurements and Real-time Seismic-Amplitude Measurements (RSAM) by using continuous wavelet transform (CWT) and cross-wavelet transform (XWT) can be useful for the interpretation and surveillance of possible eruptive events. This analysis shows that the XWT coefficients of SO_2 flux and RSAM are in good agreement with the occurrence of major eruptive events and thus may be used to indicate magma ascent into the volcano edifice.

Introduction

Surveillance of volcanoes is fundamental for hazard assessment and mitigation prior to and during periods of volcanic crisis. During the last decades significant progress has been achieved on this issue by a diversity of multi-parametric surveillance approaches. Seismicity is still being considered one of the most reliable parameters for monitoring volcanic activity; hence it is probably the most popular monitoring tool used by volcanologists (e.g. Tilling 2008; D'Alessandro et al. 2013). Volcanic gas emissions play also an important role in volcanic surveillance (e.g. Casadevall et al. 1983; Burton et al. 2007; Symonds et al. 1994) since eruptions are often heralded by increments of volcanic SO_2 emissions, which originate from the ascent of fresh magma to shallower crustal levels.

Measuring sulphur dioxide (SO_2) emissions has been successfully achieved using ground-based remote sensing techniques like the correlation spectrometer (COSPEC)(Hoff and Millan 1981), mobile and scan DOAS (Galle et al. 2002; Edmonds et al. 2003; Galle et al. 2010; Burton et al. 2009) and more recently, SO_2 cameras (Mori and Burton 2006). The NOVAC (Network for Observation of Volcanic and Atmospheric Changes) project is monitoring the SO_2 fluxes of about 20 volcanoes around the world using optical scan DOAS instruments (NOVAC instruments) (Galle et al. 2010). This instrumental setup has produced a wealth of semi-continuous SO_2 flux measurements and thus permits to combine SO_2 emissions data in near real time jointly e.g. with seismic signals. The potential of combining seismic and SO_2 measurements as a surveillance tool has been demonstrated for different scenarios (e.g. Olmos et al. 2007; Conde et al. 2013; Nadeau et al. 2011). The recently enhanced activity occurring at San Cristobal makes it a suitable study case for conducting a joint analysis of seismic and gas measurements by using cross wavelet transform in order to assert the underlying processes leading to eruptive events.

Background

San Cristobal volcano is a basaltic-to-andesite stratovolcano located in north western Nicaragua approximately 15 km north-east of the city of Chinandenga (12.70°N 87.0°W; Fig. 1). Volcanic activity at San Cristóbal is characterized by a persistently strong open-vent and fumarolic degassing, as stated by previous studies summarized in Table 1 (Rivera et al. 2009; Fischer von Mollard 2013; Mather et al. 2006; Barrancos et al. 2008). San Cristobal exhibits cyclical transitions between periods of quiescent degassing and substantial increases of the gas emission rates during the onset of eruptive events that are mostly characterized by minor-to-moderate explosive eruptions causing ash fallouts. These

transitions have occurred at a higher rate during the last 2 years with VEI 1- VEI 2 eruptive events occurring approximately twice a year (Smithsonian-Institution 2014).

METHODOLOGY

SO_2 flux measurements

SO_2 flux measurements were made by two NOVAC instruments installed on the west flank of San Cristóbal volcano (Fig. 1). The instrument acquires UV-scattered sunlight spectra by scanning along a vertical plane spanning 180˚ from one horizon to the other in angular steps of 3.6˚. The principal component is a spectrometer (Ocean Optics®, S2000), which operates in the wavelength range 280 - 425 nm divided into 2048 channels yielding a spectral resolution of approximately 0.6 nm. The instrument runs during daylight hours, and the signal-to-noise ratio is improved by adding 15 spectra and adjusting automatically the exposure time in order to avoid light saturation in the spectrometer detector. Under clear sky conditions it is possible to acquire approximately 60 measurements per day.

The SO_2 column amount was retrieved from the spectra for each angular step, applying DOAS in the wavelength region of 310–322 nm (Platt and Stutz 2008), where the SO_2 absorption cross section still has a pronounced signature and low sensitivity to scattering and straylight (Johansson 2009; Galle et al. 2010). More advanced details about the NOVAC instruments and column retrievals are described in Galle et al. (2010) and Edmonds et al. (2003).

In order to determine the SO_2 flux, geometrical information of the plume is required in addition to the gas columns as shown on Eq.1 from Hoff and Millan (1981).

$$\mathbf{Flux} = \mathbf{W_s} * |\mathbf{cos}(\mathbf{W_d} - \mathbf{compass})| * \mathbf{P_H} * \sum_{\mathbf{i=0}}^{\mathbf{N-1}} |\mathbf{tan}\boldsymbol{\alpha}_{\mathbf{i+1}} - \mathbf{tan}\boldsymbol{\alpha}_{\mathbf{i}}| * \boldsymbol{VCD_i} \quad (1)$$

Where $\mathbf{VCD_i}$ is the SO_2 vertical columns density estimated at the angular step $\boldsymbol{\alpha_i}$, which corresponds to the angle between the column and the zenith. **Ws** and $\mathbf{W_d}$ are the wind speed and plume direction at the plume height ($\mathbf{P_H}$), **compass** is the direction perpendicular to the plane of scanning. The plume at San Cristobal volcano predominantly bends over after leaving the crater; thus P_H was assumed to be the same as the crater height (1745 m.a.s.l.), while the plume direction was geometrically calculated by combining plume height and the scanning angles α which show the strongest absorption. The plume (wind) speed was obtained from the weather forecast model GFS, provided by the National Ocean and Atmospheric Administration (NOAA).

The uncertainty of the flux measurements using DOAS is the result of a combination of error sources including spectroscopy, local weather conditions and inaccuracies in the estimation of the plume geometry. Previous studies have

provided a statistical approach in order to quantify the measurement error (e.g. Mather et al. 2006; Rivera et al. 2009; Galle et al. 2010), and even more recently there have been constraints about the radiative transfer error (Kern et al. 2010).

Considering the proximity of the instruments to the emission source and the very well defined plume signatures in most of the scans, the estimated total measurement error is 35% assuming optimal weather conditions. The time series exhibits a trend akin to the different levels of volcanic activity; however, the differences between successive data samples lead to a relatively high level of variability during single days, which tends to be higher during periods of enhanced degassing. In view of the uneven sampling rate and the variability of the individual measurements, our SO_2 flux time series is restrained to the daily average of the gas emissions, in order to accentuate the long-term variations.

SO_2 flux pre-processing

Although the daily average of the gas emissions can be a good approximation of the flux evolution through time, the random nature of the degassing processes, ambient perturbations and measurement errors produce an unsteady daily standard deviation which can makes difficult to identify the underlying long-term variations in the degassing rate. One common mathematical approach to deal with this difficulty is to smooth the time series using the Kalman filter (Kalman 1960), which has been successfully applied for data estimation of geophysical measurements (e.g. Anderson 2001; Yan et al. 2014; Evensen 2003; Nagarajan et al. 2012). In contrast with traditional filtering techniques, which are based on the removal of "undesired components", the Kalman filter assumes a state-space (time) model estimator, and explicitly accounts for measurement -modelling errors.

Due to the stochastic nature of the variation of SO_2 fluxes through time, we have considered the random walk model (RWM) as a well-suited estimator; as it has been demonstrated in other scenarios of atmospheric measurements (Mulquiney et al. 1995), and is described in Eq. 2.

$$\boldsymbol{X_n} = \boldsymbol{X_{n-1}} + \boldsymbol{W_n} \tag{2a}$$

$$\boldsymbol{W_n} \sim \boldsymbol{N}(\boldsymbol{0}, \boldsymbol{Q}) \tag{2b}$$

$$\boldsymbol{Y_n} = \boldsymbol{X_n} + \boldsymbol{V_n} \tag{2c}$$

$$\boldsymbol{V_n} \sim \boldsymbol{N}(\boldsymbol{0}, \boldsymbol{R}) \tag{2d}$$

The Kalman filter algorithm predicts the process $\mathbf{X_n}$ (daily flux) as described on the estate equation (Eq. 2a) with its corresponding expected variability $\mathbf{W_n}$ and corrects this prediction taking into account a simplified measurement model (Eq. 2c) with its corresponding measurement noise $\mathbf{V_n}$. A fair estimation of the expected variability is probably one of the most difficult aspects for applying the Kalman filter assuming a RWM. Although many procedures have been suggested, we have considered a statistical approach, as illustrated in Myers and Tapley (1976), where **Q** is the flux variance during a period of 1 day which can be considered as a suitable approximation of expected variability $\mathbf{W_n}$. The measurement error variance **R** is assumed to be constant and estimated on the basis of the flux measurement error that was previously referred to account for 35% of daily average flux. A full description of the recursive predictor-corrector Kalman Filter algorithm applied on the RWM described can be found elsewhere (e.g. Welch and Bishop 1995; Mulquiney et al. 1995; Myers and Tapley 1976).

A comparison of the Kalman estimated SO_2 flux versus the individual daily SO_2 flux measurement during a selected period of 4 months at San Cristobal volcano is displayed in figure 2. Although the daily average tends to follow a distinct trend, the scattering of the individual points may produce undesired jumping components that can interfere with further frequency domain analysis. The smoothing the time series by mean of a Kalman filter balances a trade-off between the signal trend and its natural variability.

Seismic data

RSAM (Real Time Seismic Amplitude Measurements) (Endo and Murray 1991) were calculated from measurements of the station CRIM that belongs to the INETER seismic network and is located within the summit area of the volcano (Fig. 1). Each individual RSAM measurement corresponds to the average value of the seismic amplitude during 10 minutes; however, the averaging time was increased up to 1 day in order to make it coherent with the daily sampling rate of the SO_2 flux. The RSAM time series was pre-processed using a Kalman filter algorithm with the same approach as the one described in the previous section.

WAVELET ANALYSIS

Several methods can be applied in order to perform a joint analysis of volcanic SO_2 fluxes and RSAM. Some classical approaches such as cross-correlations and Fourier transform may produce acceptable results when considering time series with short time windows and some degree of stationarity. However, through extended periods of analysis, the

underlying volcanic processes exhibit unforeseen changes, which are associated to variations in the eruptive regime and are reflected in unforeseen changes of the spectral characteristics both of the SO_2 fluxes and RSAM time series. Correspondingly, Continuous Wavelet Transform (CWT) is a mathematical tool that decomposes a time series into time-frequency components allowing time-localisation of spectral characteristics that are statistically significant during a particular period. Due to the non-stationary nature of many geophysical and atmospheric systems, several studies have applied this time series analysis technique, predominantly in climatology (e.g. Torrence and Webster 1999; Wang and Gao 2013; Mwale and Gan 2005; Kestin et al. 1998).

The CWT $\mathbf{W_n(s)}$ can be defined as the convolution of the time series $\mathbf{X_n}$ with a scaled and translated wavelet function $\boldsymbol{\psi}\mathbf{(n/s)}$.

$$\boldsymbol{W_n(s) = \sum_{n'=0}^{N-1} X_t \, \psi \left[\frac{n'-n}{s} \delta t\right]} \quad (3)$$

Where $\boldsymbol{\delta_t}$ is the sampling period and **s** is the CWT scale (period). The spectral decomposition is achieved by discretely compressing and/or expanding the scale **s** prior to performing the convolution. The mathematical basis and details concerning the choice and design of wavelet functions is out of the scope of this article and can be found elsewhere; however, out of several possible wavelet functions, this article examines the performance of four popular wavelets: Paul, Morlet, DOG(m=2) and DOG(m=6). One of the most important criteria concerning the choice of a determined wavelet is the trade-off between time and frequency resolution; in this regard, the Morlet wavelet is highly popular in geophysical applications due to its well-balanced proportion between these two parameters(Torrence and Compo 1998).

The outcome of $\mathbf{W_n(s)}$ is an array of coefficients distributed according to their corresponding time-scale, normally displayed as a contour or temperature map where the CWT wavelets coefficient amplitude ($\mathbf{W_n}$) is plotted at their respective period (frequency) and time. The statistical significance of the coefficient amplitudes was calculated assuming that their spectral properties depict increased amplitude at lower frequencies. This spectral feature which is commonly observed in geophysical time series is normally referred as red noise and, can be modelled by a stochastic first order autoregressive (AR1) process (Allen and Smith 1996). A typical assumption is to consider that the statistical significance of wavelets coefficients is 5% (95% confidence level) against red noise(Grinsted et al. 2004).

The cross-wavelet transform (XWT) is just an extension of the CWT for performing a joint analysis of two time series by the conjugate product of their CWT, as shown in eq. 4.

$$\mathbf{W^{XY}=W^{X}W^{Y*}} \quad (4)$$

187 Unlike traditional correlation methods, XWT allows to correlate common spectra-amplitude signatures of a pair of
188 signals at localized periods. Further details of the implementation of the CWT, XWT and the 5% statistical significance
189 can be found in Torrence and Compo (1998) and Grinsted et al. (2004) respectively.
190

191 Results

192 Chronology of SO_2 degassing and seismicity

193 Fig. 3 shows a comparison between SO_2 fluxes and RSAM, outlining three periods of enhanced volcanic activity
194 characterized by moderate explosions and ash emissions. During the eruptive period by the end of December 2012, SO_2
195 emissions featured an oscillating behaviour increasing from a background of approximately 1000 $tday^{-1}$ culminating in a
196 peak value of approximately 2500 t day^{-1}. At the onset of this eruptive period (December 26), the coupling between
197 RSAM and degassing trends started to increase, gaining correlation towards the explosive events. Approximately 10
198 days after the crisis started, there were no more reports of explosive activity and SO_2 emissions gradually decreased,
199 which was additionally reflected by a decrease in correlation between the two signals. By the middle of February 2013
200 the SO_2 emissions remained relatively stable, reaching an average flux of ≈250 t day^{-1}. Unfortunately the post eruptive
201 seismicity is unknown since the seismic station stopped working during approximately 3 months, as a result of the ash
202 depositions during the eruptions. However, in view of posterior observations, it is plausible to assume that the
203 seismicity followed the decreasing trend as featured by the SO_2 emissions.
204 During May 2013, the eruptive activity resumed after a relatively abrupt exhalation event, which was clearly correlated
205 with an increase in RSAM counts, and the SO_2 flux raised from 250 to approximately 800 t day^{-1} through a period of 10
206 days before returning to its initial value. Following this precursory event, during the period 5-11 June 2013 occurred a
207 series of VEI 1 explosive events accompanied by ash emissions. However, despite the intensity of the explosions, SO_2
208 emissions increased only slightly; while in contrast, RSAM increased significantly. Afterwards, SO_2 emissions and
209 RSAM gradually returned to their pre-eruptive values.
210 Following approximately 6 months of relative calm, eruptive activity resumed again during the period comprising 15
211 January to 11 February 2014. A significant increment of the RSAM correlated well with a series of VEI 1-2 explosive
212 events and a sustained increase of the SO_2 emissions which reached a peak value of approximately 3000 t day^{-1} during
213 the explosive eruptions.

XWT joint analysis

During time windows close to and including the main eruptive events, the CWT of both time series show clear patterns of statistically significant coefficients and frequency shifts from a background periodicity of 0.1 day^{-1} to 0.35 day^{-1} (10 to 2.8 days) (Fig. 3c and d). Hence, the correlation between both times series was investigated in view of their common spectral-amplitude signatures by applying XWT, and the resultant coefficients are shown in Fig. 4a. In comparison with the individual CWT of both SO_2 fluxes and RSAM, the patterns of the statistically significant coefficients of the XWT exclusively show the features, which both time series have in common and reveal a pronounced signature. These are explicitly restricted to periods with immediate temporal proximity to evident eruptive activity. A better representation of the temporal variation is obtained by averaging the statistically significant XWT coefficients amidst their predominant periodical range (0.03-0.4 day^{-1} or 33.3-2.5 days). Fig. 4b shows that the result of the averaged XWT coefficients, and the main eruptive events are in good agreement with the averaged coefficient peaks.

Discussion

The SO_2 time series indicate that persistent degassing of San Cristobal averaged approximately <1000 t day^{-1} during the period reported in this study, while in the immediate temporal proximity of eruptive events, significant increments in the SO_2 emissions and seismicity are asserted by observing their time series and their corresponding CWT coefficients. A closer look at the grey insets of Fig. 3d, indicates that the RSAM CWT coefficients are preceding the eruptive events for a longer period in comparison to the SO_2 flux CWT coefficients. This feature can be interpreted as a precursory increment of seismic energy which may be attributed to intrusion of fresh magma batches at shallower crustal levels, resulting in an increasing permeability of degassing pathways and thus causing a subsequent increase in degassing activity. This assumption is consistent with the enhanced occurrence of tremor and long period seismicity as reported by INETER for the respective periods, and in turn reflected within the RSAM time series. Tremor and other low frequency seismic signatures have been typically associated with displacements of magma and fluids through the conduit (Chouet 1996; Julian 1994; Langer et al. 2011; Matsumoto et al. 2013; Yamamoto et al. 2002). Accordingly, a possible scenario preceding the subsequent explosive events, may involve a progressive gas exolution accompanied by magma cooling/crystallization especially in the shallower part of the magma feeding system, thus inducing an overpressure in the conduit (Stix et al. 1997; Tait et al. 1989). Another possible scenario involves a thermal interaction between the

shallow magma body and the hydrothermal system, thus, triggering a phreatic or phreatomagmatic eruption (Germanovich and Lowell 1995). In any case, either the overpressure in the conduit and/or the interaction with the hydrothermal system, may lead to the remarkable increase of the SO_2 flux that was measured prior to the subsequent explosive events. Nonetheless, the activity period comprising the exhalation event in April 2013 and its following eruption in June was slightly distinct in comparison with the eruptive events of December 2013 and February 2014. During the exhalation event, a significant pulse of SO_2 was released with little restraint as a result of the removal of material in the upper conduit due to the previous eruptions. In view of the increasing seismicity that accompanied the exhalation event, it is plausible to consider that this exhalation was the result of magma intrusion releasing gas under conditions of low pressure combined with physical obstruction. Hence, during the explosive events a relatively low SO_2 flux was measured probably because the intruding magma had exolved a substantial amount of gas. Thus in the following months before the next eruptive events, in view of the heavy rainy season, the conditions for a sealing of the upper part of the conduit and a subsequent overpressure are given. Further studies which include petrological evidence are required in order to better estimate the mechanisms behind the eruptive events described in this study.

Implications for volcanic surveillance

Despite the diversity of possible mechanisms triggering the eruptive activity at San Cristobal volcano, the CWT coefficient signals produced by each eruptive event more or less look the same: on the onset and during eruptive periods both time series show significant CWT coefficients with increased magnitudes shifted to higher frequencies. Correspondingly, from previous studies where continuous SO_2 flux and RSAM measurements were made, it has been demonstrated that by analysing the spectral content of their time series it is possible to some extent to identify the separate contributions of geophysical parameters like deformation, tremor, long period seismicity and tidal cycles (Conde et al. 2013; Saballos et al. 2014; Bredemeyer and Hansteen 2014). Moreover, the spectral content of these time series typically is not stationary. Thus major variations of their spectral signatures can be associated to anomalies, which in the case of San Cristobal volcano are in good agreement with eruptive events. Thus, the ability of the XWT for detecting common spectral anomalies of SO_2 and RSAM, makes this tool suitable for surveillance of volcanoes with a similar eruptive behaviour as San Cristobal. In addition, as described in equations 1 to 3, these algorithms are relatively easy to implement in a near-real time graphical data presentation of qualitative changes in eruptive activity.

Despite the potential of this method as a volcanic activity forecasting tool, CWT and XWT have one main limitation, since the time series are finite and CWT assumes a cyclic time series, the resulting coefficients at the border of the times series have some degree of distortion. On a CWT or XWT contour map, the area where edge distortion is neglectable is typically termed as the cone of influence (COI), which for this particular case is indicated as the black x marks of the XWT contour map shown in Fig. 4a. This limitation can be of minor importance for studies intended to perform a post-analysis of eruptive records. However, when considering the XWT of SO_2 emissions and RSAM as a potential tool for near-real time volcanic monitoring, it is necessary to notice that the most recent measurements are going to lie within the COI. Many different approaches have been suggested in order to reduce the distortion caused by the border effects in the COI. The simplest solution involves the extension of the borders in a suitable way, and some of the most common methods include zero-padding, extended padding, periodical padding and antisymmetric padding (Pacola et al. 2013; Su et al. 2011). In addition, it's important to underline that the area of the COI depends on the selected wavelet; hence, narrower wavelets have fewer distorted coefficients since the area of the COI is smaller (Torrence and Compo 1998).

We examine the distortion of the COI by combining different padding methods and different wavelets. To do this, we simulated a time series of XWT averaged coefficients derived from the SO_2-RSAM measurements, by sequentially calculating their XWT for every daily measurement within a time window containing the previous 100 measurements. The simulated time series comprises the scale averaged XWT coefficients at the end of the current time window which are distorted due to the border effect and represents a real situation when a new measurement of SO_2 and RSAM is added to the time series. Fig. 5 a, b, c and d shows the comparison, for different wavelets, of the scaled averaged XWT coefficients between the simulated time series and a standard case (Fig. 4b). After several evaluations it was found that the antisymmetric-padding produced lower errors except in the case of the wavelet DOG(m=6) where zero-padding was used instead. Although at first glance the distortion is obvious, it still resembles the qualitative variations of the averaged coefficients that are not affected by the COI. The qualitative comparisons for different wavelets are completed with the cross-correlation analysis shown in Fig. 5 (e, f, g and h). By observing the Full Width at Half Maximum (FWHM) we can state that out of the considered wavelets, Paul(Fig. 5e) and DOG(2)(Fig. 5f) have a lower distortion due to the COI effect, which is not surprising considering that these two wavelets are narrower. However, the symmetry and smoothness of the correlogram shown in Fig. 5e suggests that the Paul wavelet at least in this case is the best option

for applying averaged XWT coefficients as a qualitative forecasting tool for a joint analysis of SO_2 emissions and RSAM.

Conclusions

The continuous activity at San Cristobal volcano, noticeable by its persistent degassing and seismicity have allowed us to propose an novel approach for a joint analysis of SO_2 fluxes and RSAM described by different activity stages. Initially we have described a SO_2 flux pre-processing approach implemented by using the Kalman filter which takes into account measurement errors and the estimated variability. Several studies with the aim of better constraining flux measurement errors are under progress, and this simplified statistical approach for SO_2 flux time series can be easily adapted to further improve error analysis and thus provide more accurate statistics. Furthermore, it has been shown that analysing SO_2 fluxes and RSAM by observing their CWT coefficients provides additional insights that are not so obvious at first glance. As a result, it was graphically easy to identify the increasing seismic energy preceding major eruptive events, which may be associated with magma emplacement to shallower crustal levels.

Although joint analysis of seismicity and emissions have been applied in several scenarios, the analysis presented here demonstrates the use of CWT and CWT for interpretation and surveillance of eruptive events. In the case of San Cristobal volcano, the contours of the XWT coefficients and the peaks of the averaged coefficients correlate well with the reported eruptive events. We have also demonstrated the possibility of implementing a routine for near-real time observations by analysing the errors and distortion due to the border effect. In this case, by using narrower wavelets, such as Paul, is possible to reduce this artefact. Although such techniques can be applied to other volcanos with continuous degassing, an extensive analysis of previous degassing and seismic reports is necessary in order to identify a suitable threshold that allows to define significant changes of the ongoing volcanic activity.

In summary, this paper demonstrates another application of using permanent DOAS instruments for continuous measurements of SO_2 in complement to the widely used seismic monitoring techniques.

Acknowledgements

This work was supported by the Swedish International Development Agency (SIDA), in coordination with Instituto Nicaragüense de Estudios Territoriales (INETER). Further support was received from the Helmholtz Foundation through the “Remote Sensing and Earth System Alliance” (HA-310/IV010). We would like to thank the staff from INETER for their friendly support and in particular for the assistance and dedication provided by David Chavarría and

Hoffman Sanchez.

References

Allen M, Smith LA (1996) Monte Carlo SSA: Detecting irregular oscillations in the Presence of Colored Noise. J Climate 9 (12):3373-3404. doi:citeulike-article-id:8829360

Anderson JL (2001) An Ensemble Adjustment Kalman Filter for Data Assimilation. Monthly Weather Review 129 (12):2884-2903. doi:10.1175/1520-0493(2001)129<2884:AEAKFF>2.0.CO;2

Barrancos J, Roselló JI, Calvo D, Padrón E, Melián G, Hernández PA, Pérez NM, Millán MM, Galle B (2008) SO2 emission from active volcanoes measured simultaneously by COSPEC and mini-DOAS. Pure and Applied Geophysics 165 (1):115-133

Bredemeyer S, Hansteen T (2014) Synchronous degassing patterns of the neighbouring volcanoes Llaima and Villarrica in south-central Chile: the influence of tidal forces. Int J Earth Sci (Geol Rundsch) 103 (7):1999-2012. doi:10.1007/s00531-014-1029-2

Burton M, Allard P, Mure F, La Spina A (2007) Magmatic gas composition reveals the source depth of slug-driven strombolian explosive activity. Science 317 (5835):227-230. doi:10.1126/science.1141900

Burton MR, Caltabiano T, Murè F, Salerno G, Randazzo D (2009) SO2 flux from Stromboli during the 2007 eruption: Results from the FLAME network and traverse measurements. Journal of Volcanology and Geothermal Research 182 (3-4):214-220. doi:10.1016/j.jvolgeores.2008.11.025

Casadevall T, Rose W, Gerlach T, Greenland LP, Ewert J, Wunderman R, Symonds R (1983) Gas emissions and the eruptions of Mount St. Helens through 1982. Science 221 (4618):1383-1385

Conde V, Bredemeyer S, Duarte E, Pacheco J, Miranda S, Galle B, Hansteen T (2013) SO2 degassing from Turrialba Volcano linked to seismic signatures during the period 2008–2012. Int J Earth Sci (Geol Rundsch):1-16. doi:10.1007/s00531-013-0958-5

Chouet BA (1996) Long-period volcano seismicity: its source and use in eruption forecasting. Nature 380 (6572):309-316

D'Alessandro A, Scarfì L, Scaltrito A, Di Prima S, Rapisarda S (2013) Planning the improvement of a seismic network for monitoring active volcanic areas: The experience on Mt. Etna. Advances in Geosciences 36:39-47

Edmonds M, Herd RA, Galle B, Oppenheimer CM (2003) Automated, high time resolution measurements of SO2 flux at Soufrière Hills Volcano, Montserrat. Bulletin of Volcanology 65 (8):578-586

Endo ET, Murray T (1991) Real-time Seismic Amplitude Measurement (RSAM): a volcano monitoring and prediction tool. Bulletin of Volcanology 53 (7):533-545

Evensen G (2003) The Ensemble Kalman Filter: Theoretical formulation and practical implementation. Ocean Dynamics 53 (4):343-367

Fischer von Mollard K (2013) Variationen in den SO2-Ausstößen des San Cristóbal Vulkans zwischen 2006 und 2012 ermittelt anhand von bodenbasierter UV-Spektometrie (Mini-DOAS). University of Kiel,

Galle B, Johansson M, Rivera C, Zhang Y, Kihlman M, Kern C, Lehmann T, Platt U, Arellano SR, Hidalgo S (2010) Network for Observation of Volcanic and Atmospheric Change (NOVAC) - A global network for volcanic gas monitoring: Network layout and instrument description. J Geophys Res 115 (D5):D05304. doi:10.1029/2009jd011823

364 Galle B, Oppenheimer C, Geyer A, McGonigle AJS, Edmonds M, Horrocks L (2002) A miniaturised ultraviolet
365 spectrometer for remote sensing of SO2 fluxes: A new tool for volcano surveillance. Journal of
366 Volcanology and Geothermal Research 119 (1-4):241-254
367 Germanovich LN, Lowell RP (1995) The mechanism of phreatic eruptions. Journal of Geophysical Research:
368 Solid Earth 100 (B5):8417-8434. doi:10.1029/94JB03096
369 Grinsted A, Moore JC, Jevrejeva S (2004) Application of the cross wavelet transform and wavelet coherence
370 to geophysical times series. Nonlinear Processes in Geophysics 11 (5-6):561-566
371 Hoff RM, Millan MM (1981) Remote SO2 mass flux measurements using COSPEC. Journal of the Air
372 Pollution Control Association 31 (4):381-384
373 Johansson M (2009) Application of Passive DOAS for Studies of Megacity Air Pollution and Volcanic Gas
374 Emissions. PhD thesis Chalmers University of Technology
375 Julian BR (1994) Volcanic tremor: Nonlinear excitation by fluid flow. Journal of Geophysical Research: Solid
376 Earth 99 (B6):11859-11877. doi:10.1029/93JB03129
377 Kalman RE (1960) A New Approach to Linear Filtering and Prediction Problems. Transactions of the ASME –
378 Journal of Basic Engineering (82 (Series D)):35-45. doi:citeulike-article-id:347166
379 Kern C, Deutschmann T, Vogel L, Wöhrbach M, Wagner T, Platt U (2010) Radiative transfer corrections for
380 accurate spectroscopic measurements of volcanic gas emissions. Bulletin of Volcanology 72 (2):233-
381 247. doi:10.1007/s00445-009-0313-7
382 Kestin TS, Karoly DJ, Yano JI, Rayner NA (1998) Time-frequency variability of ENSO and stochastic
383 simulations. Journal of Climate 11 (9):2258-2272
384 Langer H, Falsaperla S, Messina A, Spampinato S, Behncke B (2011) Detecting imminent eruptive activity at
385 Mt Etna, Italy, in 2007–2008 through pattern classification of volcanic tremor data. Journal of
386 Volcanology and Geothermal Research 200 (1–2):1-17.
387 doi:http://dx.doi.org/10.1016/j.jvolgeores.2010.11.019
388 Mather TA, Pyle DM, Tsanev VI, McGonigle AJS, Oppenheimer C, Allen AG (2006) A reassessment of current
389 volcanic emissions from the Central American arc with specific examples from Nicaragua. Journal of
390 Volcanology and Geothermal Research 149 (3-4):297-311. doi:10.1016/j.jvolgeores.2005.07.021
391 Matsumoto S, Shimizu H, Matsushima T, Uehira K, Yamashita Y, Nakamoto M, Miyazaki M, Chikura H (2013)
392 Short-term spatial change in a volcanic tremor source during the 2011 Kirishima eruption. Earth,
393 Planets and Space 65 (4):323-329
394 Mori T, Burton M (2006) The SO2 camera: A simple, fast and cheap method for ground-based imaging of
395 SO2 in volcanic plumes. Geophysical Research Letters 33 (24):L24804. doi:10.1029/2006GL027916
396 Mulquiney JE, Norton JP, Jakeman AJ, Taylor JA (1995) Random walks in the kalman filter: Implications for
397 greenhouse gas flux deductions. Environmetrics 6 (5):473-478. doi:10.1002/env.3170060509
398 Mwale D, Gan TY (2005) Wavelet Analysis of Variability, Teleconnectivity, and Predictability of the
399 September–November East African Rainfall. Journal of Applied Meteorology 44 (2):256-269.
400 doi:10.1175/JAM2195.1
401 Myers K, Tapley BD (1976) Adaptive sequential estimation with unknown noise statistics. Automatic
402 Control, IEEE Transactions on 21 (4):520-523. doi:10.1109/TAC.1976.1101260
403 Nadeau PA, Palma JL, Waite GP (2011) Linking volcanic tremor, degassing, and eruption dynamics via SO2
404 imaging. Geophysical Research Letters 38 (1):L01304. doi:10.1029/2010GL045820
405 Nagarajan K, Judge J, Monsivais-Huertero A, Graham WD (2012) Impact of assimilating passive microwave
406 observations on root-zone soil moisture under dynamic vegetation conditions. IEEE Transactions on
407 Geoscience and Remote Sensing 50 (11 PART1):4279-4291
408 Olmos R, Barrancos J, Ivera CR, Barahona F, López DL, Henriquez B, Hernández A, Benitez E, Hernández PA,
409 Pérez NM, Galle BO (2007) Anomalous emissions of SO2 during the recent eruption of Santa Ana
410 volcano, El Salvador, Central America. Pure and Applied Geophysics 164 (12):2489-2506

411 Pacola ER, Quandt VI, Schneider FK, Sovierzoski MA (2013) The Wavelet Transform Border Effect in EEG
412 Spike Signals. In: Long M (ed) World Congress on Medical Physics and Biomedical Engineering May
413 26-31, 2012, Beijing, China, vol 39. IFMBE Proceedings. Springer Berlin Heidelberg, pp 593-596.
414 doi:10.1007/978-3-642-29305-4_155
415 Platt U, Stutz J (2008) Differential Optical Absorption Spectroscopy (DOAS), Principle and Applications.
416 Springer Verlag, Heidelberg. doi:10.1007/978-3-540-75776-4
417 Rivera C (2009) Application of Passive DOAS using Scattered Sunlight for quantification of gas emissions
418 from anthropogenic and volcanic sources. Chalmers tekniska högskola,
419 Rivera C, Garcia JA, Galle B, Alonso L, Yan Z, Johansson M, Matabuena M, Gangoiti G (2009) Validation of
420 optical remote sensing measurement strategies applied to industrial gas emissions. International
421 Journal of Remote Sensing 30 (12):3191-3204. doi:10.1080/01431160802558808

422

423 Saballos J, Conde V, Malservisi R, Connor C, Álvarez J, Muñoz A (2014) Relatively short-term correlation
424 among deformation, degassing, and seismicity: a case study from Concepción volcano, Nicaragua.
425 Bulletin of Volcanology 76 (8):1-11. doi:10.1007/s00445-014-0843-5
426 Smithsonian-Institution (2014) http://www.volcano.si.edu/volcano.cfm?vn=344020.
427 Stix J, Torres RC, Narváez M L, Cortés J GP, Raigosa JA, Gómez M D, Castonguay R (1997) A model of
428 vulcanian eruptions at Galeras volcano, Colombia. Journal of Volcanology and Geothermal Research
429 77 (1–4):285-303. doi:http://dx.doi.org/10.1016/S0377-0273(96)00100-X
430 Su H, Liu Q, Li J (2011) Alleviating border effects in wavelet transforms for nonlinear time-varying signal
431 analysis. Advances in Electrical and Computer Engineering 11 (3):55-60
432 Symonds R, Rose WI, Bluth GJS, Gerlach TM (1994) Volcanic-gas studies; methods, results, and applications.
433 Reviews in Mineralogy and Geochemistry 30 (1):1-66
434 Tait S, Jaupart C, Vergniolle S (1989) Pressure, gas content and eruption periodicity of a shallow,
435 crystallising magma chamber. Earth and Planetary Science Letters 92 (1):107-123.
436 doi:http://dx.doi.org/10.1016/0012-821X(89)90025-3
437 Tilling RI (2008) The critical role of volcano monitoring in risk reduction. Advances in Geosciences 14:3-11
438 Torrence C, Compo GP (1998) A Practical Guide to Wavelet Analysis. Bulletin of the American
439 Meteorological Society 79 (1):61-78. doi:10.1175/1520-0477(1998)079<0061:APGTWA>2.0.CO;2
440 Torrence C, Webster PJ (1999) Interdecadal Changes in the ENSO–Monsoon System. Journal of Climate 12
441 (8):2679-2690. doi:10.1175/1520-0442(1999)012<2679:ICITEM>2.0.CO;2
442 Wang P, Gao J (2013) Extraction of instantaneous frequency from seismic data via the generalized Morse
443 wavelets. Journal of Applied Geophysics 93:83-92
444 Welch G, Bishop G (1995) An Introduction to the Kalman Filter. University of North Carolina at Chapel Hill,
445 Yamamoto M, Kawakatsu H, Yomogida K, Koyama J (2002) Long-period (12 sec) volcanic tremor observed at
446 Usu 2000 eruption: Seismological detection of a deep magma plumbing system. Geophysical
447 Research Letters 29 (9):43-41
448 Yan Y, Barth A, Beckers JM (2014) Comparison of different assimilation schemes in a sequential Kalman
449 filter assimilation system. Ocean Modelling 73:123-137

450

451

452

453

Date	SO_2 (t day^{-1})	Reference
November-2003	800±190	a
March-2006	317±274	b
November-2006	1406±805	c
2007	515±517	d
2008	244±203	d
2009	1515±891	d
2010	893±727	d
2011	627±235	d
2012	1489±671	d

454

455 Table 1. Compilation of previous measurements of SO_2 emissions at San Cristobal volcano (a) Mather et al. (2006), (b)
456 Barrancos et al. (2008), (c) Rivera (2009), (d) Fischer von Mollard (2013)

457

458

459

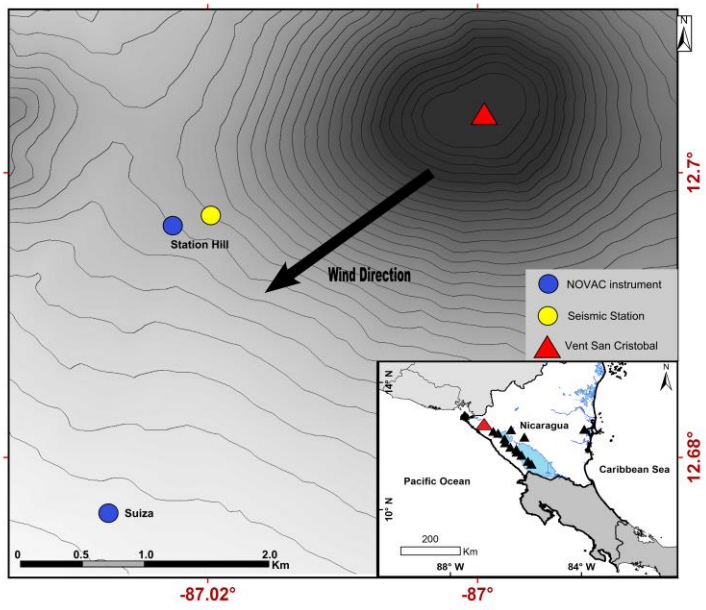

460

461 Fig. 1 Map showing the location of the NOVAC instruments and seismic station on the Southwestern flank of San
462 Cristobal volcano. Inset map of the volcanic arc in Nicaragua (black triangles).

463

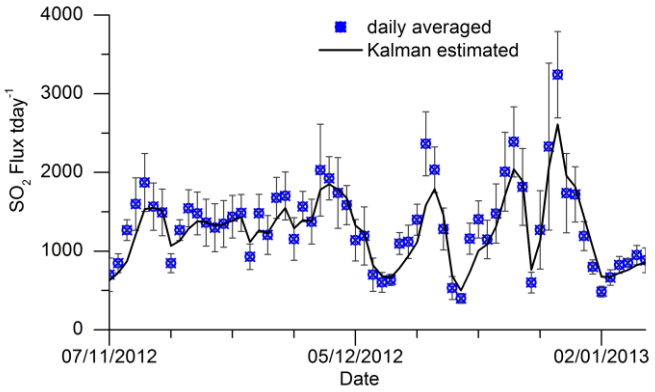

464

465 Fig. 2. Comparison between daily average SO_2 fluxes and the Kalman estimated fluxes from November 2012 to
466 January 2013.

467

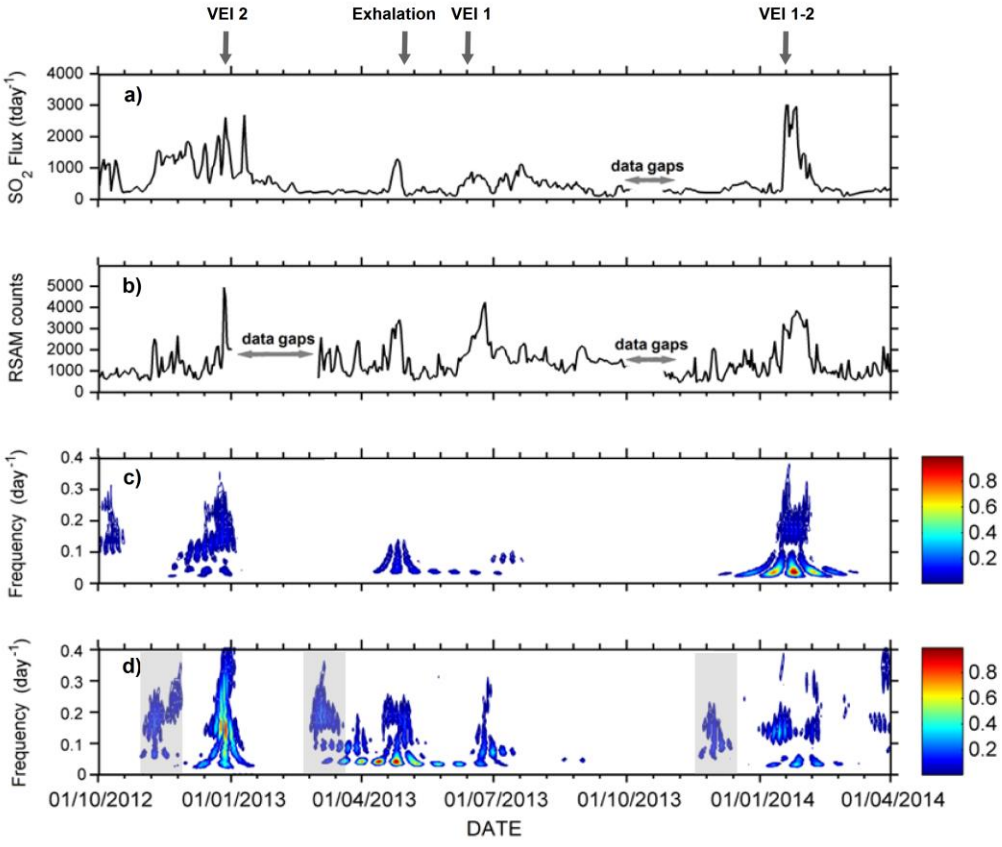

468

469 Fig. 3. Estimated fluxes and RSAM with their respective wavelet transform at San Cristobal during the period: October
470 2012 to April 2014. (a) SO_2 fluxes. (b) RSAM counts. (c) SO_2 CWT power spectrum coefficients. (d) RSAM CWT
471 power spectrum coefficients with precursory periods highlighted by the grey insets. The CWT power spectrum

coefficients were obtained by using the Morlet wavelet. The map colour of the wavelet coefficients against the white background corresponds to the coefficients greater than 95% significant test for red noise; and the arrows mark periods of enhanced eruptive activity.

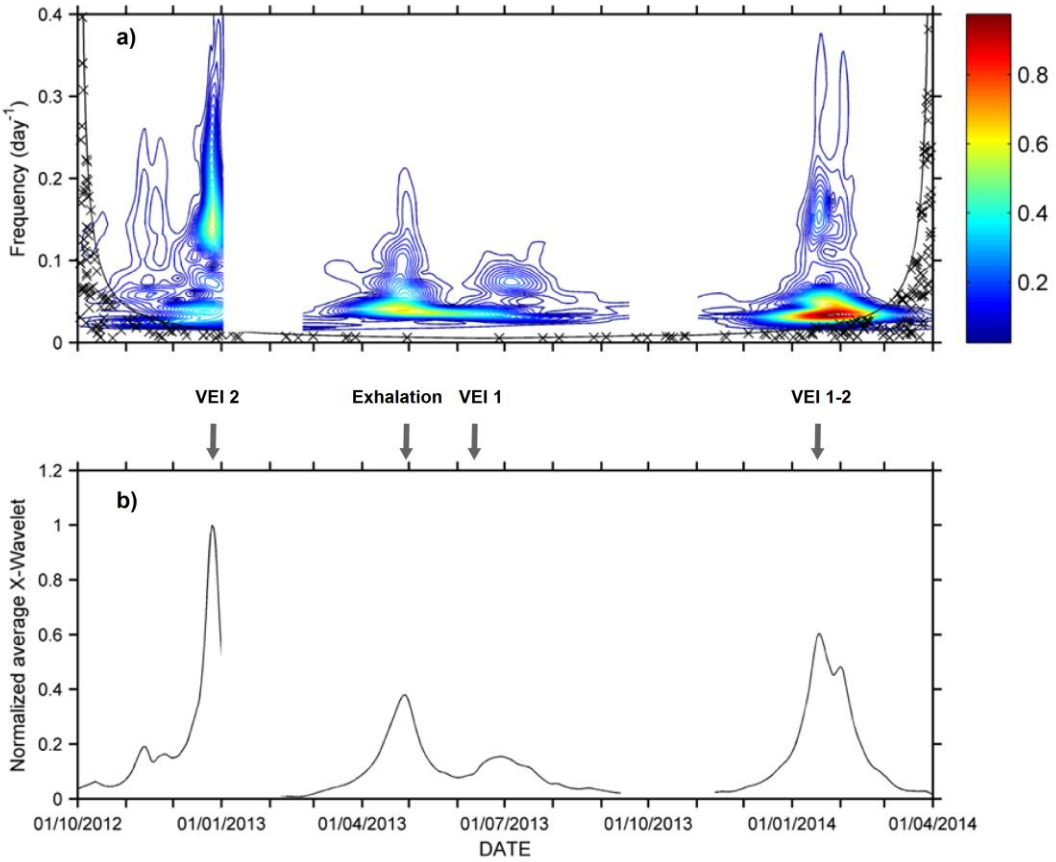

Fig. 4. a) XWT power spectrum coefficients between the SO_2 fluxes and RSAM (Fig. 3a and b). The map colour of the cross-wavelet coefficients against the white background corresponds to the coefficients greater than 95% significant test for red noise. b) XWT Scale-averaged coefficients. The arrows mark the onset of periods of enhanced eruptive activity which were shown on Fig. 3. The discontinuities correspond to measurement gaps.

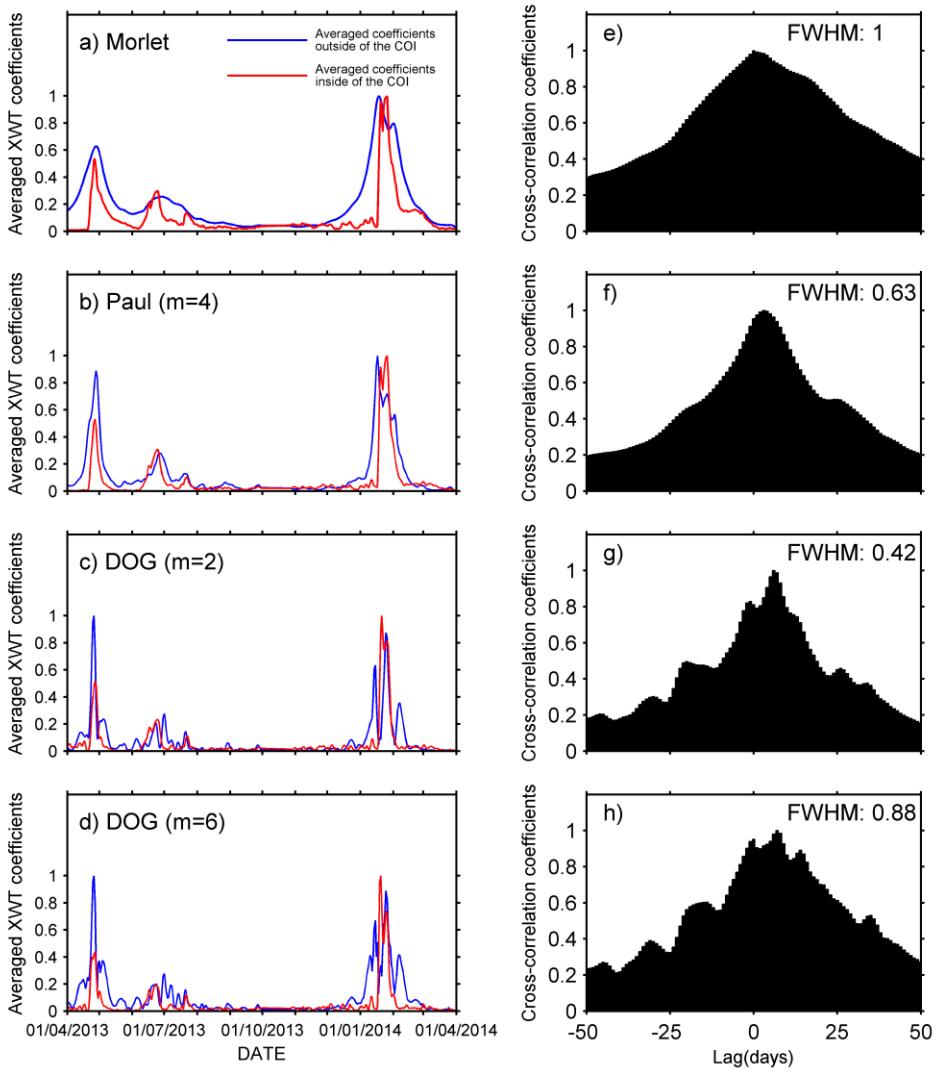

Fig. 5 Comparison of the XWT and border effects. In the right column, the blue line corresponds to the XWT scale-averaged coefficients unperturbed by the COI. The red line corresponds to the averaged coefficients lying in the left boundary of the COI. The pair of time series in (a), (b), (c) are padded using antisymmetric padding (ASYM) except in (d) whereas zero-padding is used instead. In the left column, the cross-correlations between each pair of time series on the right side. The Full Width at Half Maximum (FWHM) of the different wavelets is relative to the FWHM of the Morlet wavelet. The lower FWHMs suggest that the wavelets Paul (f) and DOG(m=2)(g) are less affected by the border effect.